Modeling 3D hybrid battery-electrolyzer nickel electrodes

Möller-Gulland, Robin; van Ommen, J. Ruud; Mulder, Fokko M.

DOI
10.1016/j.xcrp.2025.102545

Publication date
2025

Document Version
Final published version

Published in
Cell Reports Physical Science

Citation (APA)
Möller-Gulland, R., van Ommen, J. R., & Mulder, F. M. (2025). Modeling 3D hybrid battery-electrolyzer nickel electrodes. *Cell Reports Physical Science*, *6*(5), Article 102545. https://doi.org/10.1016/j.xcrp.2025.102545

Cell Reports
Physical Science

Article

Modeling 3D hybrid battery-electrolyzer nickel electrodes

Graphical abstract

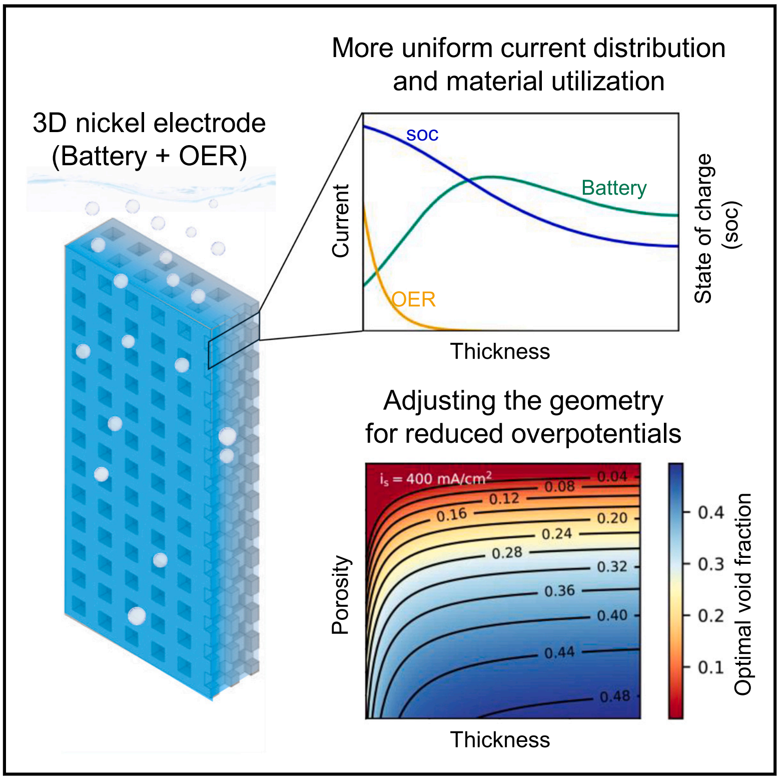

Highlights

- 3D electrodes enhance material use and ensure a more uniform current distribution
- We determine the optimal void fraction balancing ionic conductivity and surface area
- The charging efficiency for battery use is significantly improved
- Overpotentials for oxygen evolution are reduced

Authors

Robin Möller-Gulland,
J. Ruud van Ommen, Fokko M. Mulder

Correspondence

robin.gulland@rwth-aachen.de (R.M.-G.),
f.m.mulder@tudelft.nl (F.M.M.)

In brief

Möller-Gulland et al. introduce a 1D model describing the current and potential distribution in 3D nickel electrodes that integrates battery and electrolysis functionality. Based on this model, they develop a method to determine the optimal void fraction and demonstrate how improved ionic conductivity improves both battery performance and oxygen evolution.

Möller-Gulland et al., 2025, Cell Reports Physical Science *6*, 102545
May 21, 2025 © 2025 The Author(s). Published by Elsevier Inc.
https://doi.org/10.1016/j.xcrp.2025.102545

CellPress

Please cite this article in press as: Möller-Gulland et al., Modeling 3D hybrid battery-electrolyzer nickel electrodes, Cell Reports Physical Science (2025), https://doi.org/10.1016/j.xcrp.2025.102545

Cell Reports
Physical Science

CellPress
OPEN ACCESS

Article

Modeling 3D hybrid battery-electrolyzer nickel electrodes

Robin Möller-Gulland,[1,*] **J. Ruud van Ommen,**[2] **and Fokko M. Mulder**[2,3,*]
[1]Materials for Energy Conversion and Storage, Delft University of Technology, 2629HZ Delft, the Netherlands
[2]Product and Process Engineering, Delft University of Technology, 2629HZ Delft, the Netherlands
[3]Lead contact
*Correspondence: robin.gulland@rwth-aachen.de (R.M.-G.), f.m.mulder@tudelft.nl (F.M.M.)
https://doi.org/10.1016/j.xcrp.2025.102545

SUMMARY

An integrated battery-electrolyzer stores renewable electricity as a battery and produces hydrogen when overcharged. This dual application requires electrode concepts that ideally enhance both battery and electrolysis operation without compromising either. One such concept is 3D structured electrodes including channels that improve ionic conductivity and material utilization as well as facilitating bubble removal during electrolysis. In this work, we first develop a 1D model of a porous sintered nickel electrode that takes the void fraction of the 3D geometry into account and allows for the determination of the current and potential distribution for both battery charging and oxygen evolution. An optimized void fraction that maximizes the reactive surface area for oxygen evolution is determined, and we discuss under what circumstances a 3D geometry is beneficial. Finally, we show how the improved ionic conductivity of 3D electrodes also results in more homogeneous battery charging, increasing charging efficiency in nickel electrodes.

INTRODUCTION

Climate change poses significant risks to modern society, threatening food security,[1] disrupting biodiversity,[2] exacerbating socioeconomic inequalities,[3] and causing more frequent and severe weather events.[4] It is widely recognized that anthropogenic CO_2 emissions are the major cause of an increase in average global temperatures since the start of the industrialization. Mitigating climate change by reducing CO_2 emissions calls for the transition to renewable energy sources such as wind and solar. However, their daily and seasonal variability requires the integration of both short- and long-term energy storage.[5,6]

The integrated alkaline Ni-Fe battery and electrolyzer (battolyser^{TM}) introduced by Mulder et al.[7] integrates both short- and long-term energy storage in a single device. It is based on a nickel-iron battery in which the nickel and the iron electrodes not only function as battery electrodes but also generate oxygen and hydrogen, respectively, when fully charged. This integrated battery-electrolyzer can compensate for diurnal variations in the energy supply by charging at times of low energy prices (e.g., during oversupply of wind and solar) and discharging when the energy prices are high (e.g., at peak times in the evening). In contrast to designated battery technologies such as Li ion, the battolyser can still store energy in the form of hydrogen even when fully charged. This can then be stored and used for seasonal energy needs, for transportation, and as a feedstock for the steel and chemical industry.

However, electrodes employed in conventional nickel-iron batteries are not designed for this dual application of battery energy storage and alkaline electrolysis. On the contrary, oxygen and hydrogen evolution has been considered as parasitic side reactions that decrease the battery charging efficiency, deplete water in the electrolyte, and pose an explosion hazard. While conventional nickel and iron battery electrodes can perform electrolysis efficiently at low current densities,[7] their transport properties become limiting at high current densities. Therefore, new types of hybrid electrodes are required that combine a high battery storage capacity and rate capability with efficient electrolysis at industrially relevant current densities.

Besides the intrinsic activity of an electrocatalyst, structural properties of the electrode, such as the thickness, porosity, and reactive surface area, play a significant role in the electrode performance.[8,9] The larger the reactive surface area over which the applied current is distributed, the lower the local current density and thus the overpotential is going to be. Thick, porous electrodes made from sintered metals, foams, or felts loaded with catalyst and/or active battery material offer a high surface area and battery capacity per square centimeter of superficial electrode area (height × width). However, the utilization of this surface area, and thus the effectively used electrode thickness, is limited by the ohmic losses incurred by the ionic electrolyte resistance within the electrode.

Additive manufacturing of 3D structured porous electrodes allows for the realization of complex geometries with multiscale interconnected porosity, which can be rationally designed to meet the requirements for a specific application and operating conditions.[10–13] As shown by Roy et al.,[10] the integration of macroscopic electrolyte-filled voids in the porous electrode structure (e.g., channels) improves electrolyte accessibility and thus reduces the ionic resistance within the electrode. The

Please cite this article in press as: Möller-Gulland et al., Modeling 3D hybrid battery-electrolyzer nickel electrodes, Cell Reports Physical Science (2025), https://doi.org/10.1016/j.xcrp.2025.102545

benefits of such 3D electrodes have been demonstrated for both battery applications[12,14–16] and water electrolysis.[17–20] For the latter, a periodic 3D structure facilitates bubble removal compared to, for example, a stochastically structured nickel foam.[17] Bubbles displace the conductive electrolyte and cover catalytically active sites, resulting in increased ohmic losses, an inhomogeneous current distribution, and higher overpotentials.[21,22] Therefore, strategies to effectively remove bubbles are essential in increasing the energy efficiency of an electrolyzer.[23] Due to the advantages for both battery and electrolysis operation, periodically structured 3D porous electrodes are a promising option for an integrated battery-electrolyzer.

On the other hand, the benefits of a 3D geometry must be weighed against the reduction in surface area and battery capacity compared to a planar electrode. Whether or not a 3D geometry is suitable has to be decided under consideration of the electrode porosity, thickness, current density, and overpotentials for both the oxygen evolution reaction (OER) and the (dis)charging battery reaction. Modeling the current distribution and overpotential across the electrode thickness can aid in the understanding of how structural electrode properties affect performance. Such models have been covered extensively in the literature for planar porous nickel battery electrodes under consideration of (dis)charging kinetics and concentration gradients for both OH^- and O_2.[24–27] However, none of these models can be applied directly to account for the additional macroscopic 3D geometry. Recently, Li et al.[28] introduced a density-based topology optimization framework that optimizes the full-cell design in electrochemical energy storage devices, including the individual 3D geometries of both the anode and the cathode. The resulting interdigitated designs result in an increase in energy storage density of up to 750% compared to traditional planar electrode geometries. Similar approaches in topology optimization have been demonstrated for supercapacitors[29] and redox-flow batteries.[30] However, these studies do not account for two reactions in parallel with different relevant overpotentials as is the case for battery-electrolyzer electrodes.

A key parameter required for modeling the current distribution in electrodes is the ionic conductivity. A planar porous electrode consists of the solid, partially metallic, phase and the electrolyte within the pores that conducts the ions. A low porosity, i.e., a low electrolyte volume within the electrode, will result in reduced ion mobility, i.e., ionic conductivity, compared to the bulk electrolyte. In addition, ion mobility is affected by the tortuosity of the pores, which is a measure of how convoluted the path of a pore is. A convoluted path through the electrode increases the distance an ion must travel, which effectively reduces the ionic conductivity. However, microscopic properties such as the porosity and tortuosity will vary throughout the electrode, resulting in a locally changing ionic conductivity. In effective medium theory, instead of accounting for this microscopic heterogeneity, average values for the porosity and tortuosity are assumed to be homogeneous throughout the electrode. With this assumption, an effective ionic conductivity, κ_{eff}, can be defined using the Bruggeman relation[31,32]:

$$\kappa_{eff} = \kappa\varepsilon^{\gamma}, \qquad \text{(Equation 1)}$$

where κ and ε are the bulk electrolyte conductivity and the electrode porosity, respectively. The Bruggeman exponent, γ, takes the tortuosity of the pores into account.[33]

A 3D structured porous electrode can be considered as hierarchically porous where the pores and 3D features (e.g., channels) constitute a micro- and macroporosity, respectively. Here, we describe the macroporosity with the void fraction Θ, which represents the volume fraction of the electrode occupied by open 3D features such as channels. The void fraction varies across the electrode and is defined by the electrode geometry. For complex electrode geometries, modeling the current distribution then requires computationally expensive 3D models that describe this specific geometry. However, in order to determine limits for the void fraction, a fast method is required that does not have to take the specific electrode geometry into account. To this end, we define an average effective ionic conductivity, $\kappa_{eff,3D}$, throughout the electrode that expands the Bruggeman relation to take the void fraction into account. We then derive a 1D differential equation in dimensionless form that describes the potential and current distribution for the OER and the charging reaction (CR) for sintered 3D nickel electrodes. By solving this differential equation numerically for varying current densities, electrode thicknesses, and void fractions, we find a simple relationship between the electrode utilization and the dimensionless voltage drop for the OER. Based on this, we develop a methodology to determine the optimal electrode void fraction that maximizes the reactive surface area and thus minimizes electrode polarization for the OER. Furthermore, we show how the increased effective ionic conductivity in 3D electrodes results in a more homogeneous current distribution and how this is beneficial for the charging efficiency and rate capability of the battery. The modeling results presented in this work are in good agreement with experimental findings detailed in a complementary paper[34] in this issue of *Cell Reports Physical Science*, particularly in Figures 5 and 7.

RESULTS AND DISCUSSION

Oxygen evolution

In order to describe the current and potential distribution for the OER within the porous electrode, we follow the methodology of Daniel-Bek[35] and Posey[36] employed for a 1D electrode model. Here, the electrode is considered as a system of idealized pores filled with electrolyte embedded within a conductive matrix. Material properties such as the specific surface area, porosity, electrolyte conductivity, etc., are considered as uniform throughout the electrode. We assume further that the reactant concentration within the pores remains constant over time and do not take the effects of concentration polarization into account. In practice, this assumption applies for the following cases: (1) when the electrolyte is highly concentrated and well mixed (e.g., in a flow-through configuration) and (2) the first moments after the OER is started, before gradients in reactant concentration can form. Effects of oxygen bubbles, such as the reduction of the effective electrolyte conductivity and coverage of electrochemically active surface area, are not considered.

Please cite this article in press as: Möller-Gulland et al., Modeling 3D hybrid battery-electrolyzer nickel electrodes, Cell Reports Physical Science (2025), https://doi.org/10.1016/j.xcrp.2025.102545

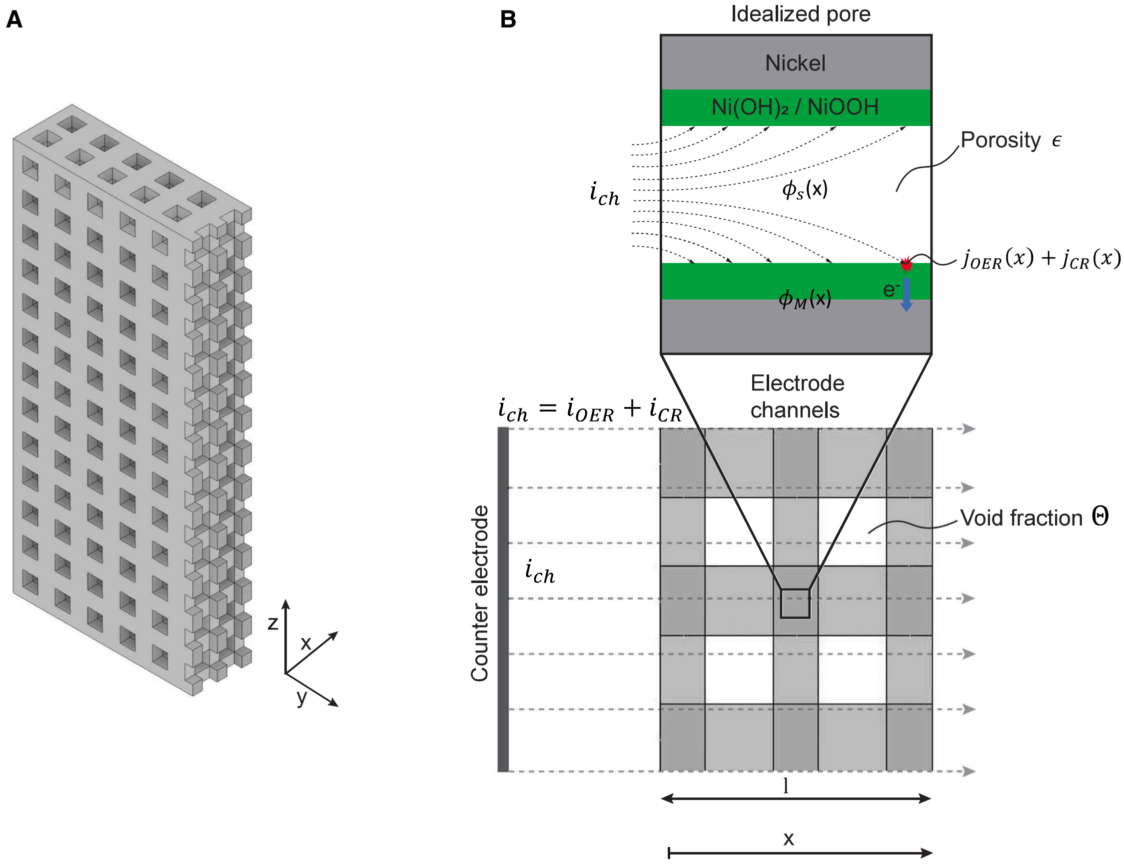

Figure 1. Illustration of the 3D electrode structure

(A) Cross section of a 3D electrode showing channels in the x, y, and z directions.

(B) Schematic of potentials and electrochemical reactions in an idealized porous 3D structured sintered nickel electrode charged at a current i_{ch}. The electrode channels constitute the macroscopic void fraction Θ. At the walls of the micropores, charging of the active material $Ni(OH)_2$/NiOOH (CR) and oxygen evolution (OER) occur with the local partial current densities $j_{CR}(x)$ and $j_{OER}(x)$, respectively. Due to both OER and CR occurring in parallel, the total charging current i_{ch} is split between the respective currents going toward the OER (i_{OER}) and CR (i_{CR}). For a fully charged electrode, $i_{ch} = i_{OER}$.

As shown in Figure 1, the total current flows from the counter-electrode across the length of the pores. Due to the limited conductivity of the solution, the ionic current flow results in a gradient in the solution potential $\phi_S(x)$ across the pore length. For a metal phase with a sufficiently low electrical resistivity compared to the ionic resistivity in the solution phase, we can assume that there is no gradient in the potential of the metal phase, ϕ_M. Electrochemical oxygen evolution occurs at the interface between the solution phase and the conductive pore walls and is driven by the difference in their respective potentials, $\Delta\phi(x) = \phi_M - \phi_S(x)$. The rate of oxygen evolution is determined by the overpotential $\eta_{OER}(x)$ with respect to the equilibrium potential $E_{0,OER}$:

$$\eta_{OER}(x) = \phi_M - \phi_S(x) - E_{0,OER}. \qquad \text{(Equation 2)}$$

Due to the gradient in the solution potential, the overpotential, and therefore the rate of oxygen evolution, decreases across the depth of the pore. In the absence of mass transfer limitations and for high anodic overpotentials, the local current density for oxygen evolution, $j_{OER}(x)$, can be described by the simplified Butler-Volmer equation:

$$j_{OER}(x) = j_{0,OER}\exp\left(\frac{\alpha_{a,OER}F}{RT}\eta_{OER}(x)\right), \qquad \text{(Equation 3)}$$

where $j_{0,OER}$ and $\alpha_{a,OER}$ are the OER exchange current density and anodic transfer coefficient, respectively. As a result of oxygen evolution, the ionic current, i_s, in the electrolyte decreases across the depth of the pore:

$$i_S(x) = i_{OER} - S\int_0^x j_{OER}(x')dx'. \qquad \text{(Equation 4)}$$

S and i_{OER} represent the electrochemically active surface area per unit length and the applied current, respectively. With Ohm's law, assuming a constant electrolyte concentration, the relation between ionic current and the solution potential is given by

$$\frac{1}{A_{el}}\left[i_{OER} - S\int_0^x j_{OER}(x')dx'\right] = \kappa\frac{d\phi_S}{dx} = -\kappa\frac{d\eta_{OER}}{dx}. \qquad \text{(Equation 5)}$$

Please cite this article in press as: Möller-Gulland et al., Modeling 3D hybrid battery-electrolyzer nickel electrodes, Cell Reports Physical Science (2025), https://doi.org/10.1016/j.xcrp.2025.102545

Differentiation of Equation 5 yields[35,36]

$$\frac{d^2\eta_{OER}}{dx^2} = \frac{S}{\kappa A_{el}} j_{OER}(x), \qquad \text{(Equation 6)}$$

where A_{el} describes the average cross-sectional electrolyte area and κ represents the electrolyte conductivity. Compared to a conventional, non-3D structured electrode, a 3D electrode replaces some of the porous electrode volume with open structures that are filled with electrolyte. These open structures, such as the channels shown in Figure 1, can be considered as macroscopic pores. In order to describe this macroscopic porosity, we introduce the void fraction θ as the ratio of the open volume (e.g., channel volume), V_{ch}, to the total electrode volume, V_{tot}: $\theta = V_{ch}/V_{tot}$. In practice, the void fraction will vary in all three spatial dimensions depending on the electrode geometry. Instead, we consider the void fraction as an average value that is uniform throughout the electrode, analogous to other electrode parameters such as porosity and surface area. The resulting model allows for more general estimates of the current and potential distribution depending on the void fraction, irrespective of the specific geometry. The average electrolyte cross-sectional area of the porous electrode, A_{el}, is determined by the electrode porosity ε and the void fraction θ of the 3D electrode. By rewriting κA_{el}, we can define an effective electrolyte conductivity for a 3D electrode, $\kappa_{eff,3D}$:

$$\kappa A_{el} = \kappa[(1-\theta)\varepsilon^{\gamma} + \theta]A = \kappa_{eff,3d}\ A, \qquad \text{(Equation 7)}$$

wherein A refers to the superficial electrode area and γ denotes the Bruggeman exponent. For a conventional electrode, i.e., for $\theta = 0$, Equation 7 describes the Bruggeman equation for the effective electrolyte conductivity commonly employed for the description of porous electrodes.[26,32,37] While the larger open volume of 3D electrodes increases the effective electrolyte conductivity, the resulting reduction in porous electrode material reduces the electrochemically active surface area. With the specific surface area for a conventional electrode S_0, the reduced specific surface area of the 3D electrode is described by $S = S_0(1-\theta)$. Overall, taking the 3D geometry into account, Equation 6 can be rewritten as

$$\frac{d^2\eta_{OER}}{dx^2} = \frac{S_0(1-\theta)}{\kappa_{eff,3D}\ A} j_{OER}(x). \qquad \text{(Equation 8)}$$

The equations above can be simplified by adopting a dimensionless notation as shown by Posey.[36] We define a reduced length $\xi = x/l$, where l is the electrode thickness; a reduced reaction rate $\rho_{OER}(\xi) = j_{OER}(\xi)/j_{0,OER}$; a reduced total current $I_{OER} = i_{OER}/i_{0,OER}$ with the exchange current density of the porous electrode $i_{0,OER} = S_0(1-\theta)lj_{0,OER}$; the resistance parameter $K_{OER} = (i_{0,OER}lF)/(\kappa_{eff,3D}ART)$; and the reduced overpotential $\Phi_{OER}(\xi) = [F\eta_{OER}(\xi)]/RT$. With this dimensionless notation Equation 8 can be rewritten as

$$\frac{d^2\Phi_{OER}(\xi)}{d\xi^2} = K_{OER}\rho_{OER}(\xi), \qquad \text{(Equation 9)}$$

with

$$\rho_{OER}(\xi) = e^{\alpha_{a,OER}\ \Phi_{OER}(\xi)}. \qquad \text{(Equation 10)}$$

The potential and current distribution over the thickness of a porous (3D) electrode can be determined by solving Equation 9 for $\Phi(\xi)$ with the following boundary conditions:

$$\left.\frac{d\Phi_{OER}}{d\xi}\right|_{\xi=0} = -K_{OER}I_{OER}, \left.\frac{d\Phi_{OER}}{d\xi}\right|_{\xi=1} = 0. \qquad \text{(Equation 11)}$$

Battery charging and electrolysis in parallel

In battery-electrolyzer nickel electrodes, the CR of the active material and the OER occur simultaneously during charging. Equation 4 can be extended to include both CR and OER in parallel:

$$i_S(x) = i_{ch} - S\int_0^x [j_{OER}(x') + j_{CR}(x')]\,dx', \qquad \text{(Equation 12)}$$

from which follows

$$\frac{d^2\eta_{OER}}{dx^2} = \frac{S_0(1-\theta)}{\kappa_{eff,3D}\ A}[j_{OER}(x) + j_{CR}(x)]. \qquad \text{(Equation 13)}$$

The porosity and electrochemically active surface area are assumed to be constant throughout charging. In order to solve this differential equation, we require terms for the local current densities for both the CR and the OER. The overall CR of $Ni(OH)_2$ to NiOOH is given by

$$Ni(OH)_2 + OH^- \xrightarrow{\text{charging}} NiOOH + H_2O + e^-. \qquad \text{(Equation 14)}$$

We assume that the active material loaded into the porous structure of sintered nickel forms a homogeneous film on the pore walls. During charging, protons and electrons are released from the interlamellar sheets of $Ni(OH)_2$ and diffuse through the bulk of the active material to the electrolyte interface and current collector, respectively. Reversely, protons and electrons are intercalated during discharging.[38] The kinetics for both the CR and oxygen evolution are known to vary with the proton concentration at the surface of the active material film contacting the electrolyte.[38,39] Here, we neglect the diffusive mass transfer resistances of protons and assume that there is no gradient in proton concentration across the thickness of the active material film. Therefore, the surface proton concentration equals that of the bulk. Furthermore, we do not take differences in electronic conductivity between the highly conductive nickel scaffold and the active material into account. The state of charge (SOC), $soc(x)$, can be expressed using the average proton concentration $c_H(x)$ in the nickel hydroxide film:

$$soc(x) = 1 - \frac{c_H(x)}{c_{H,\max}}, \qquad \text{(Equation 15)}$$

where $c_{H,\max}$ denotes the maximum proton concentration, i.e., when the active material is fully discharged. Ta and Newman determined that the exchange current density for oxygen evolution on pure nickel hydroxide films increases linearly with the

Please cite this article in press as: Möller-Gulland et al., Modeling 3D hybrid battery-electrolyzer nickel electrodes, Cell Reports Physical Science (2025), https://doi.org/10.1016/j.xcrp.2025.102545

SOC and exhibits irreversible Tafel behavior.[39] Therefore, the local current density for oxygen evolution can be expressed as

$$j_{OER}(x) = j_{0,OER,ref}\left(\frac{c_{OH}}{c_{OH,ref}}\right)^2 soc(x)\ \exp\left(\frac{\alpha_{a,OER}F}{RT}\eta_{OER}(x)\right). \quad \text{(Equation 16)}$$

For the CR, we adapt the kinetic expression used by Fan and White[25] and De Vidts and White[24]:

$$j_{CR}(x) = 2\ j_{0,CR,ref}\left[\frac{c_{OH}}{c_{OH,ref}}\ [1 - soc(x)]\exp\left(\frac{\alpha_{a,CR}F}{RT}\eta_{CR}(x)\right) - soc(x)\exp\left(-\frac{\alpha_{c,CR}F}{RT}\eta_{CR}(x)\right)\right] \quad \text{(Equation 17)}$$

Here, c_{OH} is the electrolyte concentration, and $c_{OH,ref}$ is the reference electrolyte concentration at which the exchange current densities of the CR, $j_{0,CR,ref}$, and oxygen evolution, $j_{0,OER,ref}$, were measured. We assume that there are no changes in reactant concentration over time, so that c_{OH} does not change across the depth of the pores. The overpotential for each reaction is given by

$$\eta_{OER}(x) = \phi_M - \phi_S(x) - E_{0,OER}, \quad \text{(Equation 18)}$$

$$\eta_{CR}(x) = \phi_M - \phi_S(x) - E_{0,CR}(x). \quad \text{(Equation 19)}$$

The equilibrium potential for the battery CR, $E_{0,CR}(x)$, depends on the proton concentration and can be estimated by the Nernst equation[26]:

$$\begin{aligned} E_{0,CR}(x) &= E_{0,1/2} + \frac{RT}{F}\ ln\left(\frac{1 - \frac{c_H(x)}{c_{H,\max}}}{\frac{c_H(x)}{c_{H,\max}}}\right) \\ &= E_{0,1/2} + \frac{RT}{F}\ ln\left(\frac{soc(x)}{1 - soc(x)}\right), \end{aligned} \quad \text{(Equation 20)}$$

where $E_{0,1/2}$ represents the equilibrium potential at 50% SOC. In practice, the CR for the nickel electrode has been shown to exhibit a mixed potential due to the OER at higher states of charge.[40] In addition, the equilibrium potential is affected by structural changes and the intercalation of H_2O and ions such as OH^- and K^+ between the interlamellar sheets. These effects give rise to a hysteresis behavior resulting in different equilibrium potentials for the same SOC depending on whether the electrode is charging or discharging. Equation 20 can be modified to accommodate for the deviation from Nernstian behavior as a result of the above-described non-ideal effects.[41] Since this work considers only the CR, and modified Nernstian expressions are often developed for specific conditions and material properties, we employ the unmodified term in Equation 20 for the estimate of the equilibrium potential.

Subtracting Equation 19 from Equation 18 allows for the substitution of η_{CR} in Equation 17:

$$\begin{aligned} \eta_{CR}(x) &= \eta_{OER}(x) + E_{0,OER} - E_{0,CR}(x) \\ &= \eta_{OER}(x) + \Delta E_0(x) \end{aligned}. \quad \text{(Equation 21)}$$

By inserting Equation 21 into Equation 17, the differential equation in Equation 13 can be solved for $\eta_{OER}(x)$. Rewriting Equation 13 in the previously introduced dimensionless notation yields

$$\frac{d^2\Phi_{OER}}{d\xi^2} = K_{OER}\ \ \rho_{OER}(\xi, soc) + K_{CR}\ \ \rho_{CR}(\xi, soc), \quad \text{(Equation 22)}$$

$$\Phi_{CR}(\xi) = \Phi_{OER}(\xi) + \Delta\Phi_0(\xi), \quad \text{(Equation 23)}$$

where $\Delta\Phi_0(\xi) = F\Delta E_0(\xi)/RT$. The reduced reaction rates ρ_k, the resistance parameters K_k, and the reduced current I_k for OER and CR are defined as

$$\rho_k(\xi, soc) = \frac{j_k(\xi, soc)}{j_{0,k,ref}}, \quad \text{(Equation 24)}$$

$$K_k = \frac{S_0(1 - \theta)l^2 F j_{0,k,ref}}{\kappa_{eff,3D} ART}, \quad \text{(Equation 25)}$$

$$I_k(SOC) = \frac{i_k(SOC)}{S_0(1 - \theta)l j_{0,k,ref}}, \quad \text{(Equation 26)}$$

where k is OER for oxygen evolution or CR for the charging reaction. i_k represents the total current for either OER or CR across the entire electrode. SOC denotes the overall state of charge of the electrode, defined as

$$SOC(t) = \int_0^1 soc(\xi, t)d\xi. \quad \text{(Equation 27)}$$

Equation 22 is solved with the following boundary conditions:

$$\begin{aligned} \left.\frac{d\Phi_{OER}(\xi)}{d\xi}\right|_{\xi=0} &= -K_{OER}\ \ I_{OER}(soc) - K_{CR}\ \ I_{CR}(soc) \\ &= \frac{lFi_{ch}}{\kappa_{eff,3D}\ ART} \\ \left.\frac{d\Phi_{OER}}{d\xi}\right|_{\xi=1} &= 0 \end{aligned} \quad \text{(Equation 28)}$$

The local SOC, $soc(\xi, t)$, depends not only on the local charging current j_{CR} but also on the charging duration. Thus, the potential distribution described by Equation 22 is implicitly a function of time. If we neglect double-layer charging and assume no gradients in electrolyte composition, the profiles of potential and current are formed instantaneously. We further assume homogeneous charging across the thickness of the $Ni(OH)_2/NiOOH$ film and neglect mass transfer resistances within. Therefore, Equation 22 describes the steady-state potential and current distribution at time t. The local SOC can then be calculated after a time step Δt as

Please cite this article in press as: Möller-Gulland et al., Modeling 3D hybrid battery-electrolyzer nickel electrodes, Cell Reports Physical Science (2025), https://doi.org/10.1016/j.xcrp.2025.102545

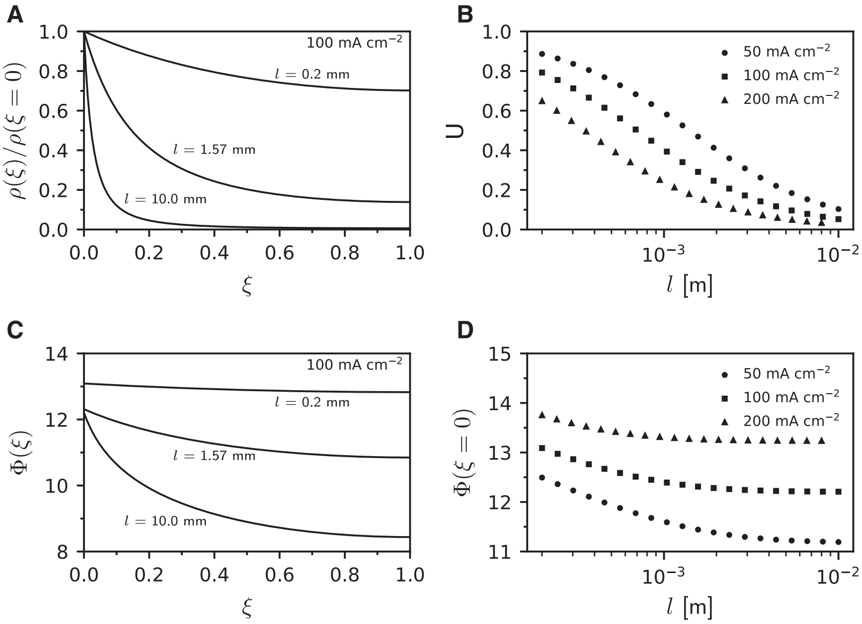

Figure 2. Current and potential distribution in non-3D electrodes

(A and C) Current distribution $\rho(\xi)/\rho(0)$ and reduced overpotential $\Phi(\xi)$ over the reduced electrode coordinate $\xi = x/l$ for a superficial current density of 100 mA/cm^2.

(B and D) Electrode utilization U as defined in Equation 30 and reduced overpotential at the front of the electrode ($\Phi(\xi) = 0$) for different electrode thicknesses and superficial current densities.

$$soc(\xi, t + \Delta t) = soc(\xi, t) + \frac{IS\rho_{CR}\, j_{0,CR,ref}}{C}\Delta t, \quad \text{(Equation 29)}$$

where C refers to the battery capacity.

Current and potential distribution in porous 3D electrodes during oxygen evolution

The larger reactive surface area of porous electrodes can effectively reduce activation overpotentials and thus increase the energy efficiency of electrochemical reactions such as the OER. Structural properties that affect electrode performance are the thickness and the porosity. While an increase in thickness enhances the overall surface area, its utilization for the electrochemical reaction is limited by the ionic resistance within the electrode pores. As a result, electrodes that are too thick can be partially inactive so that the additional surface area does not contribute to a further reduction in overpotential. Decreasing the ionic resistance, for example, by increasing the porosity and operating temperature, increases the utilization. However, an increase in porosity also decreases the surface area. Furthermore, for the here-discussed hybrid electrodes that also function as battery electrodes, porosities are typically low in order to accommodate the loaded active material that determines the energy storage capacity of the electrode. An increase in temperature is limited by the stability of the active material and cell components. While conventional alkaline electrolyzers operate at temperatures between 80°C and 90°C,[42] nickel-iron batteries are typically limited to temperatures below 45°C.[43] The 3D structure of electrodes presents an additional degree of freedom that allows for the adjustment of the ionic resistance, where the void fraction, Θ, is the equivalent of a macroscopic porosity determined by the additional open volume of the 3D features (e.g., channels). Just like the microscopic porosity, ε, of the porous electrode material, an increase in void fraction of the 3D structure decreases the ionic resistance at the cost of a reduction in reactive surface area. Therefore, the void fraction must be determined to reduce overpotentials under consideration of the applied current density as well as structural and catalytic parameters of the porous electrode material.

Conventional electrode geometry

Due to the ionic resistance, the solution potential, and therefore the overpotential, decreases across the electrode thickness. As shown in Figure 2C, the reduced overpotential is similar at the front of the electrode, $\Phi(0)$, and the back, $\Phi(l)$, if the electrode is sufficiently thin for a given current density. Accordingly, the reaction occurs over the entire electrode, albeit at a lower magnitude toward the back ($\xi = 1$). Increasing the electrode thickness results in an inhomogeneous distribution of the overpotential, shifting the reaction toward the front of the electrode. How effectively an electrode is utilized can be determined from the relative reaction rate, $\rho(\xi)/\rho(0) = j(\xi)/j(0)$. In areas where $\rho(\xi)/\rho(0)$ approaches zero, the electrode is considered inactive as a result of the too-high ionic resistance, which prevents the penetration of the reaction deeper into the electrode (Figure 2A).

Based on the definition for electrode utilization used by Rausch and Wendt ($U = l^{-1}\int_0^l j(x)/j(0)dx$),[44] we can define the utilization of an electrode via the reduced reaction rate $\rho(\xi) = j(\xi)/j(0)$ (with $i = S\int_0^x j(x')dx'$, so that $I = \int_0^1 \rho(\xi)d\xi$):

$$U = \int_0^1 \frac{\rho(\xi)}{\rho(0)}d\xi = \frac{I}{\rho(0)}. \quad \text{(Equation 30)}$$

As shown in Figure 2B, the utilization decreases not only for thicker electrodes but also for higher current densities. This is due to the increased voltage drop across the electrode thickness at higher current densities. Up to a limiting thickness, $l_{\lim}$, the electrode polarization, $\Phi(0)$, decreases. Beyond this thickness, $\Phi(0)$ does not decrease significantly (Figure 2D). This limiting thickness is commonly referred to as the reaction penetration depth.[8,32,45] It describes the thickness at which the utilization of the additional reactive surface area gained by increasing the electrode thickness is limited by the ionic resistance of the electrode. The reaction penetration depth can be defined as the characteristic length of the exponential decay of the local overpotential in a semi-infinite electrode (Figure S1).[32,45] For higher current densities, the reaction penetration depth, and thus the utilization, decreases (Figures 2B and 2D). As a result, the

Please cite this article in press as: Möller-Gulland et al., Modeling 3D hybrid battery-electrolyzer nickel electrodes, Cell Reports Physical Science (2025), https://doi.org/10.1016/j.xcrp.2025.102545

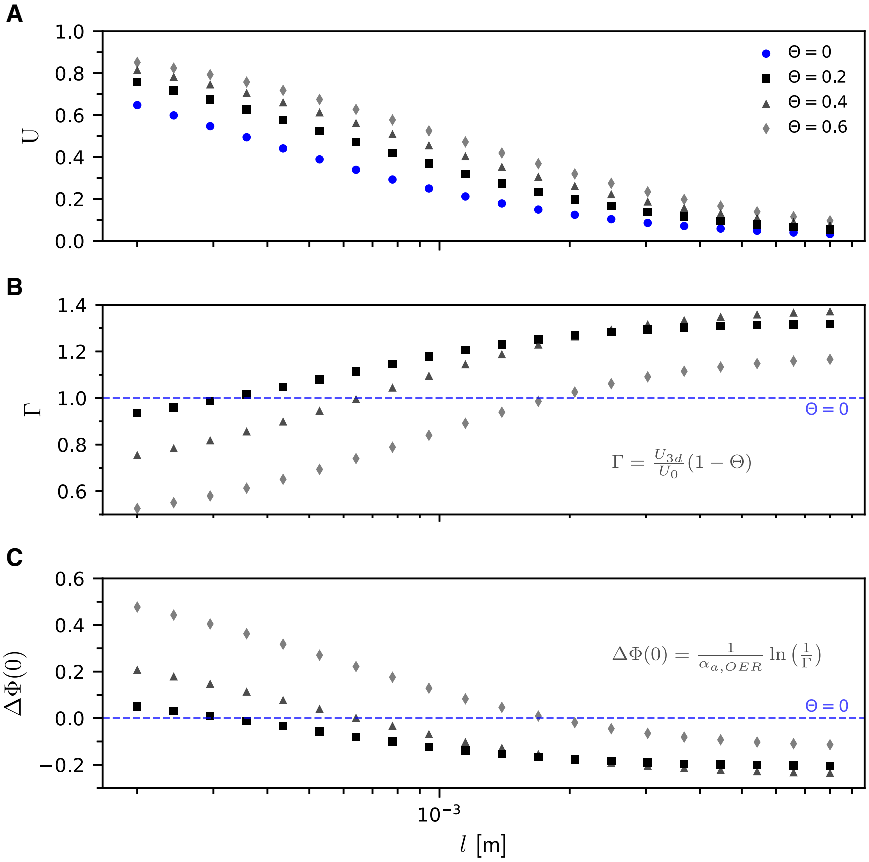

Figure 3. Effects of the void fraction and electrode thickness on utilization and polarization

Electrode utilization (A), surface enhancement (B), and difference in reduced overpotential compared to a non-3D electrode ($\Theta = 0$) at a superficial current density of 200 mA/cm^2 for different electrode thicknesses and void fractions (C). For $\Delta\Phi(0) < 0$, the reduced overpotential is lower compared to a non-3D electrode.

electrode thickness should be chosen close to the reaction penetration depth for a specific current density. Designing electrodes thicker than the reaction penetration depth results in increased material costs with no additional gain in performance. Electrodes below the reaction penetration depth reduce material costs with the caveat of higher operating costs, i.e., higher overpotentials.

Effective surface area enhancement with 3D electrodes

As shown above, in conventional electrodes, the thickness and current density are limited by the ionic resistance. Channels filled with electrolyte in a more open 3D structure decrease the ionic resistance within the electrode with the caveat of reducing the total reactive surface area. In order to reduce the activation overpotential and increase the energy efficiency, the applied current must be distributed over as large a surface area as possible. Thus, when deciding on the void fraction of a 3D electrode, we need to strike a balance between the removal and the overall improved accessibility of surface area. Using the utilization U as defined in Equation 30, the effective electrochemically active surface, $A_{R,eff}$, is given by

$$A_{R,eff} = US_0 l(1-\Theta), \qquad \text{(Equation 31)}$$

where S_0 is the surface area per unit length of a conventional electrode. In order to assess a 3D electrode compared to a conventional electrode, we define the 3D surface enhancement Γ, which is the ratio of the respective effective reactive surface areas $A_{R,eff,3D}$ and $A_{R,eff}$:

$$\begin{aligned}\Gamma &= \frac{A_{R,eff,3D}}{A_{R,eff}} \\ &= \frac{U_{3D}}{U_0}(1-\Theta) \nless 1\end{aligned} . \qquad \text{(Equation 32)}$$

Here, U_{3D} and U_0 represent the utilization of a 3D electrode and a conventional electrode, respectively. In order for a 3D electrode to be beneficial over a conventional electrode, Γ must be larger than 1. The resulting difference in electrode polarization can be derived from Tafel kinetics (see the supplemental information):

$$\begin{aligned}\Delta\Phi(0) &= \Phi_{3D}(0) - \Phi_0(0) \\ &= \frac{1}{\alpha_{a,OER}}\ln\left(\frac{1}{\Gamma}\right)\end{aligned} . \qquad \text{(Equation 33)}$$

Figure 3 shows the utilization, 3D surface enhancement, and difference in polarization of electrodes with varying void fraction and thickness at a constant superficial current density. For electrodes with a void fraction larger than 0, i.e., 3D electrodes, the utilization increases with the void fraction for all thicknesses. However, there is a limiting thickness for each void fraction at which the reduced total surface area of the 3D electrode is

Please cite this article in press as: Möller-Gulland et al., Modeling 3D hybrid battery-electrolyzer nickel electrodes, Cell Reports Physical Science (2025), https://doi.org/10.1016/j.xcrp.2025.102545

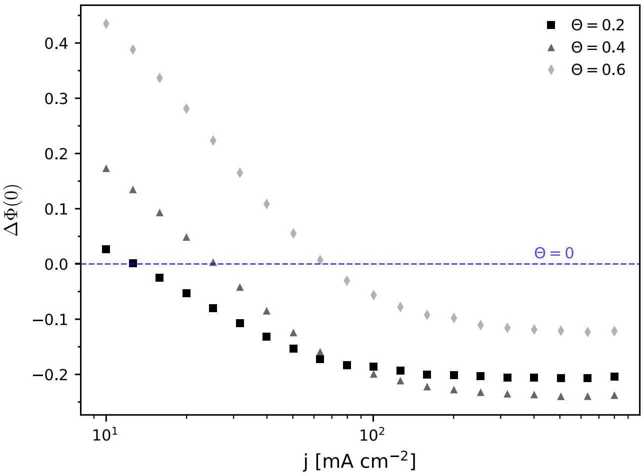

Figure 4. Polarization curves for varying electrode void fractions

Difference in reduced overpotential compared to a non-3D electrode ($\Theta = 0$) for a 5-mm-thick electrode for different superficial current densities j and void fractions Θ. For $\Delta\Phi(0) < 0$, the reduced overpotential is lower compared to a non-3D electrode.

compensated for by the decreased ionic resistance and enhanced material utilization (Figure 3B). For lower thicknesses, the effective surface area of a 3D electrode is lower compared to a conventional electrode ($\Gamma < 1$), which results in higher electrode polarization (Figure 4C). For thicknesses where $\Gamma > 1$, the increased effective conductivity results in an increase in the effectively utilized surface area, which reduces electrode polarization.

We observe a similar limit for the applied current density at a constant electrode thickness (Figure 4). It is apparent that higher void fractions are beneficial only for thicker electrodes or higher current densities, i.e., when the voltage drop across the electrode thickness is significant. However, there appears to be an upper limit to the void fraction. For the conditions shown in Figure 3 and 4, electrodes with a void fraction of 0.40 outperform those with a void fraction of 0.20 for higher thicknesses and current densities, while a void fraction of 0.60 exhibits the lowest reduction in polarization compared to a conventional electrode. Consequently, there is an optimal void fraction depending on the range of operating current density, electrode thickness, and material properties of the porous electrode scaffold.

Optimal void fraction for oxygen evolution

The results shown in Figures 2, 3, and 4 were obtained from solving Equation 9 using the finite difference method. Particularly in cases where the gradient of the overpotential is high, i.e., for high superficial current densities and thick electrodes, determining the electrode utilization and polarization requires a finer discretization, which increases computational cost. When optimizing the electrode structure, for instance, via parameter sweeps, this increases the necessary computational resources. Therefore, our goal was to determine simple relationships between the dimensionless numbers introduced above that allow for the direct calculation of the utilization and polarization for a given superficial current density and set of electrode properties. With the definition for the utilization (Equation 30), the dimensionless electrode polarization, $\Phi(0)$, is given by (with $\rho(\xi) = e^{\alpha_a \Phi(\xi)} = j(\xi)/j_0$)

$$\Phi(0) = \frac{1}{\alpha_a}\ln(\rho(0)) = \frac{1}{\alpha_a}\ln\left(\frac{I}{U}\right). \qquad \text{(Equation 34)}$$

The utilization decreases for both higher current densities and thicker electrodes (Figures 3 and 4). This is due to the voltage drop in the electrolyte across the electrode thickness. The product of the resistance parameter K and the reduced current I can be considered a dimensionless voltage drop. Plotting the utilization over KI for varying current densities, electrode porosities, void fractions, and thicknesses results in an inverse sigmoid curve as shown in Figures 5A and S3. The utilization as a function of KI can be described using a Hill function[46]:

$$U = \frac{1}{1+\left(\frac{KI}{m}\right)^k}. \qquad \text{(Equation 35)}$$

k and m represent the slope and the value of KI, where the utilization is 50%, respectively. Such an inverse sigmoid curve is also used to empirically describe the decrease in discharge capacity as a function of discharge rate in Ni-Cd batteries.[47] As shown in Figure 5, Equations 34 and 35 provide a dimensionless framework, integrating data across varying operating conditions and electrode properties. It can be used to rapidly assess when the use of 3D electrodes is the most effective and which values for the void fraction to choose. We note that, knowing this dimensionless relationship, Equation 35 can also be fit effectively over U modeled for a logarithmically spaced range of KI rather than sweeping over electrode parameters and current densities as shown here. This would further reduce the amount of computation required.

Increased 3D void fraction vs. reduction of electrode thickness

The structural electrode properties of the electrode thickness and 3D void fraction have a significant impact on utilization and polarization in that they affect the effectively available reactive surface area. Understanding how electrode thickness and 3D void fraction relate to each other is essential to arrive at guidelines for the overall electrode design. To this end, we conduct the following thought experiment: consider two electrodes of thickness l_0 with an initial void fraction of 0 and otherwise identical material properties. Both electrodes are operated at the same superficial current density j. For one electrode we decrease the thickness to l for an unchanged void fraction, and for the other we increase the void fraction while maintaining the same electrode thickness. In the first step we determine when the utilization is identical for both cases. As shown in Equation 35 and Figure 5, the utilization is determined by the factor KI. An identical value for KI will therefore result in the same value for the utilization, so that we can write

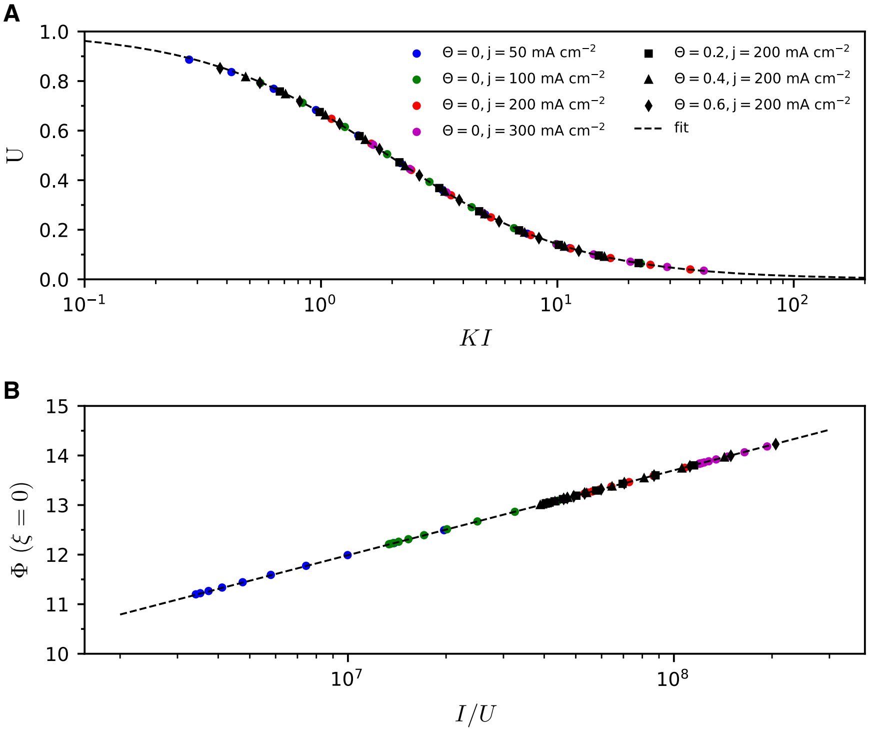

Figure 5. Dimensionless relationships between utilization U, resistance parameter K, reduced current I, and reduced overpotential at the front of the electrode $\Phi(\xi = 0)$

For each set of void fraction and current density, the polarization and current distribution were modeled for electrode thicknesses between 0.2 and 8 mm as shown in Figure 2B. The data points were fitted using Equations 35 (A) and 34 (B) with $m = 1.926$ and $k = 1.091$. KI can also be understood as a dimensionless voltage drop.

$$(KI)_{\Theta} = (KI)_{l}. \qquad \text{(Equation 36)}$$

Here, $(KI)_{\Theta}$ and $(KI)_{l}$ refer to the cases for the increase in void fraction and the decrease in electrode thickness, respectively. Inserting the expressions for the resistance parameter K and the reduced current I and rearranging for the relative reduction in electrode thickness l/l_0 yields

$$\begin{gathered} \frac{l_0 Fj}{\kappa[(1-\Theta)\varepsilon^{\gamma}+\Theta]RT} = \frac{lFj}{\kappa\varepsilon^{\gamma}RT} \\ \frac{\varepsilon^{\gamma}}{(1-\Theta)\varepsilon^{\gamma}+\Theta} = \frac{l}{l_0} \end{gathered}. \qquad \text{(Equation 37)}$$

The void fraction Θ in Equation 37 represents the void fraction that results in an equivalent utilization as a reduction of the electrode thickness by a factor of l/l_0 would for a given porosity.

For two electrodes with the same utilization, the polarization for a given superficial current density is determined by the reduced current I (Equation 34). Therefore, in order to identify the limit for the void fraction, we determine when the reduced current is equal for the cases of decreasing the electrode thickness (I_l) and increasing the void fraction (I_{Θ}):

$$\begin{gathered} I_{\Theta} = I_l \\ \frac{jA}{S_0(1-\Theta)l_0 j_{0,OER}} = \frac{jA}{S_0 l j_{0,OER}}, \\ 1-\Theta = \frac{l}{l_0} \end{gathered} \qquad \text{(Equation 38)}$$

which represents an equivalent reduction in electrode material volume, i.e., reactive surface area, for each case. Equations 36 and 38 are plotted in Figure 6A. The intersection of both curves marks the upper limit for the void fraction, $\Theta_{\max}$, where the utilization and the reduced current are identical for both the reduction in electrode thickness and the increase in void fraction. As a result, the electrode polarization is equal at this point (Equation 34). For void fractions below $\Theta_{\max}$, a 3D structured electrode results in a higher effective surface available for OER, which reduces electrode polarization. For void fractions higher than $\Theta_{\max}$, too much reactive surface area is removed compared to a reduction in electrode thickness. The 3D electrodes offer the most significant benefits over a reduction in thickness when the electrode porosity is low. For low porosities, the void fraction of the open 3D structure compensates for the reduced effective conductivity of the electrode material. As a result, $\Theta_{\max}$ decreases for higher porosities (Figure 4B). For porosities above approximately 0.62, employing a 3D electrode structure is less effective than reducing the thickness of a conventional electrode. Therefore, 3D electrodes are especially suitable for applications where the electrode porosity is lower. For example, this is the case for the hybrid battery and electrolysis electrodes discussed, where the theoretical battery capacity is determined by the amount of $Ni(OH)_2$ loaded within the pores.

Optimal void fraction for the reduction in electrode polarization

The discussion above provides an upper limit for the void fraction that is determined by the electrode porosity. However, once it has been established that a 3D structure can improve electrode performance, we need to determine a void fraction that maximizes the effectively used surface area and therefore minimizes electrode polarization. To this end, we insert Equation 35 into Equation 32, which yields an expression for the 3D surface enhancement:

$$\Gamma = \frac{1+\left(\frac{Plj}{m\varepsilon^{\gamma}}\right)^{k}}{1+\left(\frac{Plj}{m[(1-\Theta)\varepsilon^{\gamma}+\Theta]}\right)^{k}}(1-\Theta), \qquad \text{(Equation 39)}$$

Please cite this article in press as: Möller-Gulland et al., Modeling 3D hybrid battery-electrolyzer nickel electrodes, Cell Reports Physical Science (2025), https://doi.org/10.1016/j.xcrp.2025.102545

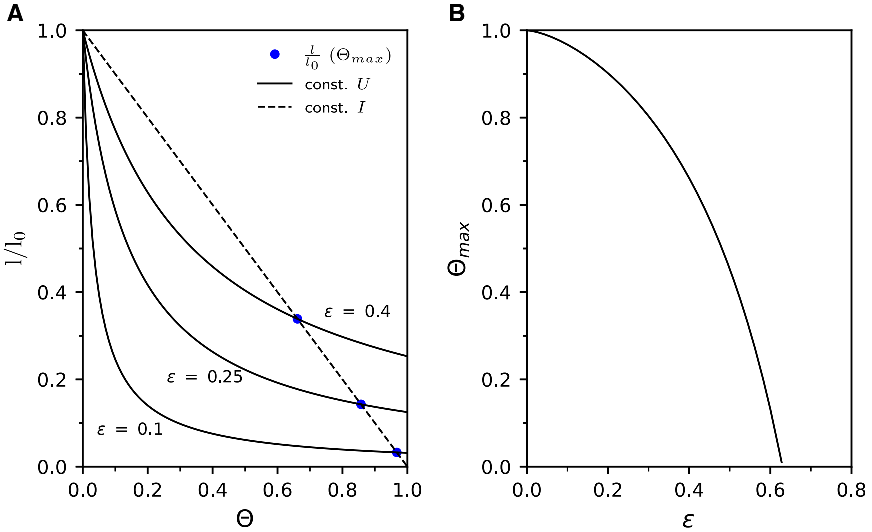

Figure 6. When is it more effective to increase the void fraction compared to decreasing the electrode thickness?

(A) Equivalent decrease in electrode thickness by a factor of l/l_0 for a given void fraction Θ that results in the same utilization U (——) and reduced current I (– – –).

(B) The maximum void fraction Θ_{max}, above which a decrease in electrode thickness is more beneficial, is defined by the intersection of the curves for constant U and I and depends on the electrode porosity ε.

where $P = F/\kappa RT$. The optimal void fraction, Θ_{opt}, results in a maximum 3D surface enhancement for a given electrolyte conductivity, porosity, electrode thickness, and superficial current density. We determine Θ_{opt} by setting the partial differential of Γ to zero and solving numerically for Θ:

$$\left.\frac{\partial \Gamma}{\partial \Theta}\right|_{\kappa,\varepsilon,l,j} = 0, 0 \leq \Theta < 1, \qquad \text{(Equation 40)}$$

where

$$\left.\frac{\partial \Gamma}{\partial \Theta}\right|_{\kappa,\varepsilon,l,j} = \frac{-k\left(\frac{Pjl}{m(\varepsilon^{\gamma}(1-\Theta)+\Theta)}\right)^{k}(1-\Theta)(\varepsilon^{\gamma}-1)}{(\varepsilon^{\gamma}(1-\Theta)+\Theta)\left(1+\left(\frac{Pjl}{m(\varepsilon^{\gamma}(1-\Theta)+\Theta)}\right)^{k}\right)^{2}} . \\ \times\left(1+\left(\frac{P\varepsilon^{-\gamma}jl}{m}\right)^{k}\right)-\frac{\left(1+\left(\frac{P\varepsilon^{-\gamma}jl}{m}\right)^{k}\right)}{\left(1+\frac{Pjl}{m(\varepsilon^{\gamma}(1-\Theta)+\Theta)}\right)^{k}} \qquad \text{(Equation 41)}$$

The optimal void fraction and the resulting absolute difference in the reduced polarization, $\left|\Delta\Phi_{opt}\right|$, are shown in Figure 7 for different porosities and electrode thicknesses at superficial current densities of 200 and 400 mA/cm^2. Generally, the optimal void fraction increases for thicker electrodes, lower porosities, and higher current densities where the ionic voltage drop across the electrode is high. This higher ionic voltage drop is mitigated by the improved ionic conductivity of the more open 3D structures with a higher void fraction. Remarkably, regardless of current density, electrode thickness, and porosity, the optimal void fraction is limited to values no higher than around 0.50. The threshold porosity above which 3D electrodes are not beneficial compared to conventional electrodes increases for higher current densities and thicker electrodes. It reaches a maximum at around 0.62, which is consistent with the porosity limit determined from the thought experiment above (Figure 6). For electrodes that exclusively perform OER, and without taking effects of bubble removal into account, a high porosity at or above this limit is preferable over a 3D structure, as it simplifies the manufacturing process. On the other hand, hybrid battery electrodes, which are used as OER electrodes when fully charged, will generally exhibit lower porosities and more active mass per area, as the battery capacity is determined by the volume of $Ni(OH)_2$ filling the pores. As a result, the here-discussed 3D electrodes are especially suitable for battery-electrolysis electrodes, where the channel structure allows for OER overpotentials comparable to those of a flat OER-only electrode with a higher porosity. In addition, the increased ionic conductivity of the channels is also expected to reduce overpotentials with respect to the battery CR.

Hybrid 3D battery and electrolysis electrodes

During charging, the battery CR, i.e., the electrooxidation of $Ni(OH)_2$ to NiOOH, is in competition with the OER. Since charge consumed by the OER instead of the CR reduces the charging efficiency, the OER has been considered a parasitic side reaction in conventional nickel battery electrodes. However, as the exchange current density for CR is orders of magnitude higher than for OER, significant OER typically first occurs at a higher SOC as long as the ionic and electrical conductivity is not limiting. Moreover, excessive gas evolution in battery cells with limited ventilation can result in pressure buildup and poses an explosion hazard when combined with the hydrogen produced at the battery anode during charging. In a hybrid battery-electrolysis system like the battolyser, on the other hand, the cells are pressure controlled and designed to mitigate the risks from gas crossover. Furthermore, a low charging efficiency can be mostly compensated for by extended periods of overcharging, i.e., electrolysis, but at the cost of increased charging potentials.

Nonetheless, fast battery charging with little gas evolution and overpotential increase until the electrode is fully charged significantly increases the flexibility and efficiency in the operation of the battolyser. In periods of rapid changes in energy price, the system can switch faster and store more energy between charging (low energy price) and discharging (high energy price). In addition, the nominal H_2/O_2 production rate is reached sooner after a period of discharging. For conventional nickel battery electrodes, the inhibition of the OER has been a central area of

Please cite this article in press as: Möller-Gulland et al., Modeling 3D hybrid battery-electrolyzer nickel electrodes, Cell Reports Physical Science (2025), https://doi.org/10.1016/j.xcrp.2025.102545

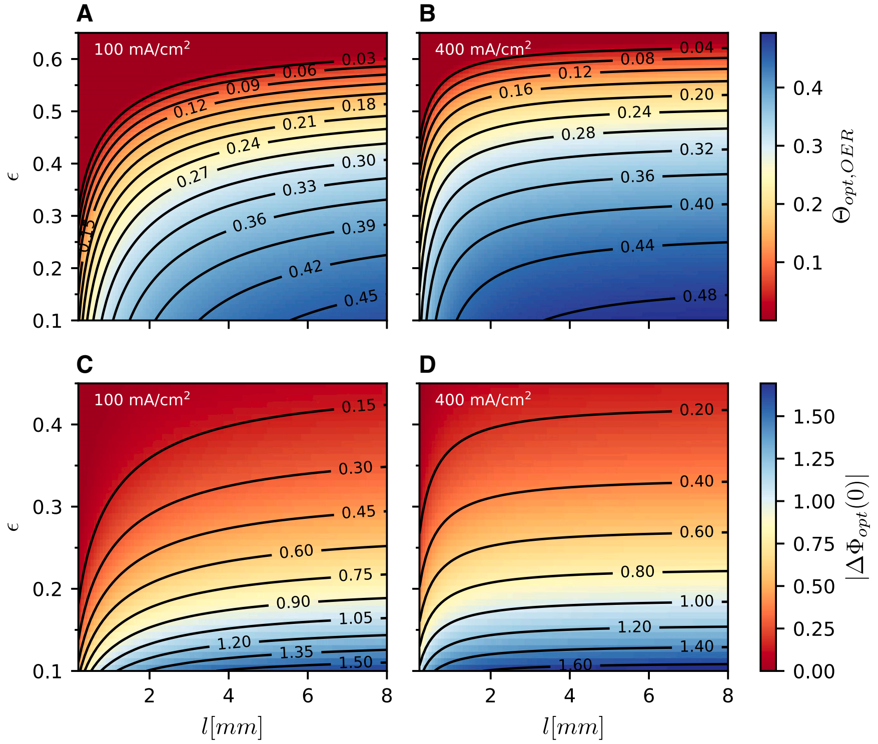

Figure 7. Optimal void fraction for the OER

Optimal void fraction ($\Theta_{opt,OER}$) with respect to the OER and the resulting absolute difference in the reduced electrode polarization ($|\Delta\Phi_{opt}|$) at varying electrode thicknesses (l) and porosities (ε) for a superficial current density of 100 (A and C) and 400 mA/cm^2 (B and D).

research over the past decades. This is typically achieved by increasing the OER potential compared to the charging potential by the addition of additives such as Co, Ca, and Cd in the active material in combination with LiOH in the electrolyte.[48–50] An increase in OER potential, i.e., the potential during overcharging, can be achieved using additives that either increase the equilibrium potential, $E_{0,OER}$, or decrease the exchange current density, $j_{0,OER}$, and the transfer coefficient, α_{OER}. However, for the here-discussed hybrid electrodes, an increase in OER potential would reduce the overall energy efficiency of the battolyser for hydrogen production. In the following, we demonstrate how a more open 3D-structured electrode, in addition to reducing OER overpotential, can increase the battery charging efficiency.

In order to determine the charging characteristics of a 3D electrode, we first determine the ideal void fraction for a specific operating current density as described above (Figure 7). For this example, we set the operating current density to 200 mA/ cm^2 for both charging and subsequent electrolysis, which is within the range of conventional alkaline electrolyzers.[51] For a 5-mm-thick electrode and a porosity of 0.25, this results in a void fraction of 0.42. Figure 8 compares the overall SOC and the faradaic efficiency for the CR (i_{CR}/i_{ch}) of the 3D electrode and a conventional electrode throughout charging and overcharging. For batteries, it is common to express the inserted charge as a fraction of the nominal capacity. A charge insertion of 0.5 C, for example, is equivalent to inserting half of the nominal capacity during charging. Since the nominal capacity of a battery is specific to a set of operating conditions (charge insertion and charge and discharge rates), we normalize the inserted charge, C_{ch}, with respect to the theoretical maximum capacity, C_{th}, which is proportional to the mass of active material loaded within the pores of the nickel substrate. At the beginning of charging, the faradaic charging efficiency is 100%, so that the entire applied current contributes to increasing the SOC of the electrode with no oxygen evolution. As a result, the SOC initially increases linearly with charge insertion. However, with an increase in SOC, oxygen evolution becomes more and more prevalent until it consumes all charge when the SOC approaches 1. The rate of change of the SOC and the faradaic charging efficiency are related by

$$\frac{dSOC}{d(C_{ch}/C_{th})} = \frac{i_{CR}}{i_{ch}} = 1 - \frac{i_{OER}}{i_{ch}}. \qquad \text{(Equation 42)}$$

A too-early onset of oxygen evolution during charging results in slower charging of the battery. Consequently, electrodes should be designed to minimize oxygen evolution until the active material is fully charged (ideal charging, Figure 8). We define the onset of oxygen evolution as the relative charge insertion where the faradaic charging efficiency decreases to below 98%. As shown in Figure 8B, this threshold is crossed after a charge insertion of 0.18 and 0.52 C for the conventional and the 3D electrode, respectively. The delay in the onset of oxygen evolution of the 3D electrode results in a faster increase in the SOC and a sharper transition to oxygen evolution compared to the conventional electrode. As a result of increased oxygen evolution, the conventional electrode requires a charge insertion of 2.8 C to reach an SOC of 85%, which constitutes a 180% increase compared to the 3D electrode.

How the electrode structure can have such a significant impact on the faradaic charging efficiency becomes clear

Please cite this article in press as: Möller-Gulland et al., Modeling 3D hybrid battery-electrolyzer nickel electrodes, Cell Reports Physical Science (2025), https://doi.org/10.1016/j.xcrp.2025.102545

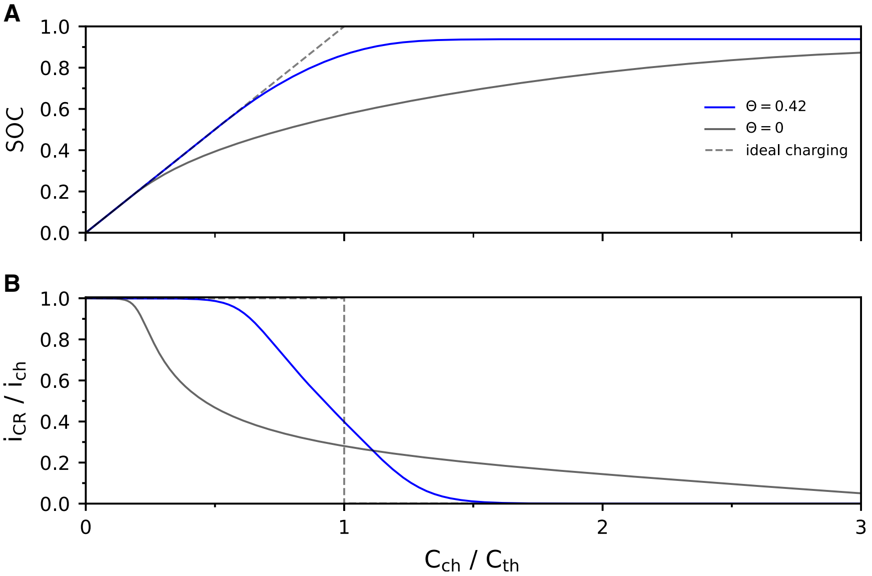

Figure 8. Charging efficiency at 200 mA/cm^2

Overall state of charge (SOC) (A) and ratio of charging current (i_{CR}) to the total applied charging current (i_{ch}) (B) over the course of charging for a non-3D electrode ($\Theta = 0$) and a 3D electrode with optimal void fraction at 200 mA/cm^2 ($\Theta = 0.42$). C_{ch} and C_{th} denote the inserted charge and the loaded capacity, respectively. Electrode thickness and porosity are 5 mm and 0.25, respectively, resulting in a loaded capacity of 172 mAh/cm^2 for the 3D electrode and 296 mAh/cm^2 for the non-3D electrode for an initial electrode porosity of 0.75 (see Equation 45). Ideal charging represents the case where no oxygen evolution occurs and the entire inserted charge goes toward charging.

when considering the current distribution within the electrode throughout charging (Figure 9). Due to the low SOC throughout the electrode, $soc(\xi)$, and the orders of magnitude higher exchange current density, CR is greatly favored over OER at the beginning of the charging process. Since the overpotentials for both CR and OER decrease over the thickness of the electrode, the magnitude of the charging current is initially highest at the front of the electrode. Therefore, the active material close to the front is charged first and gradually transitions to oxygen evolution. Because of its high exchange current density, the CR can continue at the lower overpotentials deeper within the electrode, while OER predominantly occurs in the areas with a higher SOC and close to the electrode front where overpotentials are higher. As a result, a peak in the charging current moves from the front throughout the electrode as charging continues. As can be seen in Figure 9, the lower ionic resistance of the 3D electrode leads to a more homogeneous distribution of the charging current, which delays the onset of OER to a higher overall SOC (Figure 8). For the conventional non-3D structured electrode, on the other hand, the charging current is shifted toward the front of the electrode, resulting in a faster increase in the local SOC and thus an earlier onset of OER. Due to the higher ionic resistance, current densities for OER are high at the front of the electrode, while the rest of the active material is trickle charged at low charging current densities.

While the model employed above can be used as a tool in the initial assessment of the charging performance, screening of different electrode parameters such as thickness, porosity, and void fraction, as well as operating current densities, is still computationally expensive. Here, we demonstrate a technique that can serve as a rapid initial assessment of an electrode design for a given current density. As shown above, the homogeneity of the local charging current density affects the faradaic charging efficiency and the onset of OER. For OER, we introduced a concise relationship between the electrode utilization for OER, the dimensionless resistance parameter, and the reduced current (Equation 35). However, when considering both OER and CR in parallel, the kinetic parameters are a function of the local SOC and thus vary spatially and temporally. Therefore, we consider the distribution of the local charging current density at the very beginning of charge, where the SOC is 0. Equation 17 then simplifies to

$$j_{CR}(x) = 2\; j_{0,CR,ref}\, \frac{c_{OH}}{c_{OH,ref}}\, \exp\left(\frac{\alpha_{a,CR}F}{RT}\eta_{CR}(x)\right). \qquad \text{(Equation 43)}$$

This is formally equivalent to the Tafel form used in the discussion of the current distribution for OER (Equation 3), so that the relationship between utilization, resistance parameter K, and reduced current I can be derived according to Equation 35.

As shown in Figure S2, the utilization is shifted toward higher values of KI for the CR at an SOC of 0, compared to oxygen evolution when fully charged. For Tafel kinetics, differences in the exchange current density affect only the magnitude of the overpotentials and not the current distribution and utilization.[8] We find that the observed shift in the utilization is determined by the anodic transfer coefficients of the respective reactions, which affect the parameter m in Equation 35, whereas the slope k remains mostly unchanged:

$$m_{CR} = \frac{\alpha_{a,OER}}{\alpha_{a,CR}}\, m_{OER}. \qquad \text{(Equation 44)}$$

Battery capacity in 3D electrodes

While 3D electrodes can reduce OER overpotentials and increase charging efficiency, the open channel volume reduces the porous substrate volume into which $Ni(OH)_2$ can be loaded. As a result, the theoretical maximum capacity is reduced. In the electrode design process, this caveat must be weighed against the discussed benefits of 3D structured electrodes under consideration of the operating conditions. A high areal battery capacity per unit area of membrane reduces the total amount of cells, and therefore capital expenditures, required for a target system energy storage capacity. Assuming that the nickel

Please cite this article in press as: Möller-Gulland et al., Modeling 3D hybrid battery-electrolyzer nickel electrodes, Cell Reports Physical Science (2025), https://doi.org/10.1016/j.xcrp.2025.102545

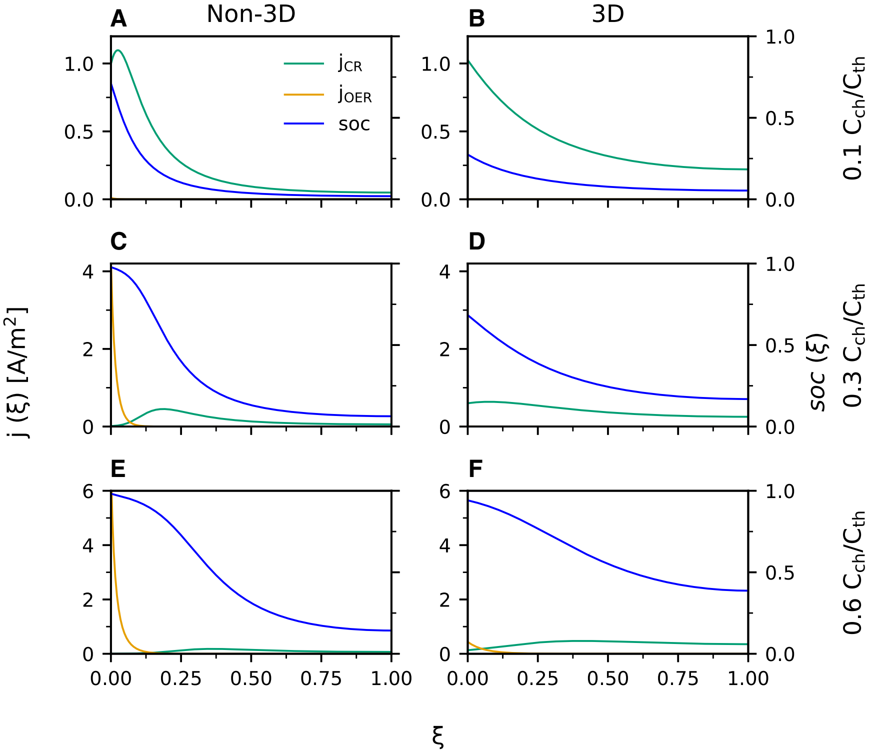

Figure 9. Current distribution and local state of charge throughout charging at 200 mA/cm^2

Local state of charge (soc) and current densities for oxygen evolution (j_{OER}) and battery charging reaction (j_{CR}) across the reduced electrode coordinate ($\xi = x/l$) for a non-3D ($\Theta = 0$) (A, C, and E) and a 3D electrode (B, D, and F) with optimal void fraction at a charge rate of 200 mA/cm^2 ($\Theta_{opt,OER} = 0.42$). These are shown for increasing charge insertion (C_{ch}) relative to the loaded capacity (C_{th}). Electrode thickness and porosity are 5 mm and 0.25, respectively, resulting in a loaded capacity of 172 mAh/cm^2 for the 3D electrode and 296 mAh/cm^2 for the non-3D electrode for an initial electrode porosity of 0.75 (see Equation 45).

substrate remains inert during battery cycling, the theoretical maximum areal battery capacity at 100% utilization is determined by the mass of active material filled into the pores of the sintered nickel scaffold with the initial porosity ε_0:

$$C_{A,th,3D} = \rho_{Ni(OH)_2}\, c_{Ni(OH)_2}\, l\,(1-\Theta)(\varepsilon_0-\varepsilon), \quad \text{(Equation 45)}$$

where $\rho_{Ni(OH)_2}$ and $c_{Ni(OH)_2}$ are the density and the weight-specific capacity (mAh/g) of the active material Ni(OH)$_2$, respectively. Figure 10 shows the optimal void fraction for OER and the resulting theoretical maximum areal capacities for varying electrode thicknesses and porosities at a superficial current density of 200 mA/cm^2. Thicker electrodes with a low final porosity and void fraction result in more active material per unit area. However, this comes at the cost of a decrease in utilization and thus charging efficiency (higher values for Kl; Figure S3).

With 172 mAh/cm^2, the theoretical maximum areal capacity of the 3D electrode discussed above ($\Theta = 0.42$) is significantly lower than that of a conventional non-3D structured electrode with 296 mAh/cm^2. Nonetheless, for the first 1.3 h of charging at 200 mA/cm^2, the charged areal capacity is higher for the 3D electrode due to the significantly improved charging efficiency (Figure S4A). For longer periods of charging and overcharging, the charged areal capacity of the conventional electrode exceeds that of the 3D electrode as more active material is trickle charged in parallel to OER. However, we note that, in practice, the extractable capacity will also depend on the discharge rate capability. This is expected to be higher in 3D electrodes due to the improved ionic conductivity resulting in a more homogeneous distribution of the discharge current.[34] Faster charging of the 3D electrode also results in a stable oxygen production rate, $\dot{m}_{O_2}$, being reached sooner (Figure S4B). This is beneficial for the balance of plant and downstream processing. Faster (re)charging and stabilization of the oxygen output improve the ability of the hybrid battery-electrolyzer to respond to fluctuations in energy price and hydrogen demand. Moreover, in the modeled time period of 4.4 h, the 3D electrode produces 15% more oxygen. The example above highlights the necessity to choose the void fraction under consideration of the required OER efficiency and production rate, areal capacity, and current density. Generally, a 3D electrode with a high void fraction is beneficial at higher current densities for CR and OER and when the battery-electrolyzer switches more frequently between charging/electrolysis and discharging. In addition, the 3D structure can be designed to facilitate bubble removal, which reduces bubble-induced overpotentials.[17,18] On the other hand, at low current densities and long uninterrupted periods of overcharging, the improved ionic conductivity of 3D electrodes with a high void fraction may not justify the loss in areal battery capacity. For increasingly thick electrodes with a high areal capacity, however, charging at such a low current density increases the charging duration. Overall, the 3D geometry and its void fraction present a novel degree of freedom that allows for tuning of battery-electrolyzer electrodes across a spectrum between conventional battery electrodes with a high energy density and combined battery-electrolysis electrodes with a high power density (Figure S5).

In this work, we develop a 1D mathematical model in dimensionless notation that describes the current and potential distribution in 3D battery-electrolyzer electrodes during charging and oxygen evolution. To this end, we expand the Bruggeman relation to define an effective ionic conductivity, $\kappa_{eff,3D}$, that includes the void fraction constituted by the electrode channels. While the reduced ionic resistance of a more open 3D geometry results in a more homogeneous current distribution and increases electrode utilization, the lower reactive surface area can increase

Please cite this article in press as: Möller-Gulland et al., Modeling 3D hybrid battery-electrolyzer nickel electrodes, Cell Reports Physical Science (2025), https://doi.org/10.1016/j.xcrp.2025.102545

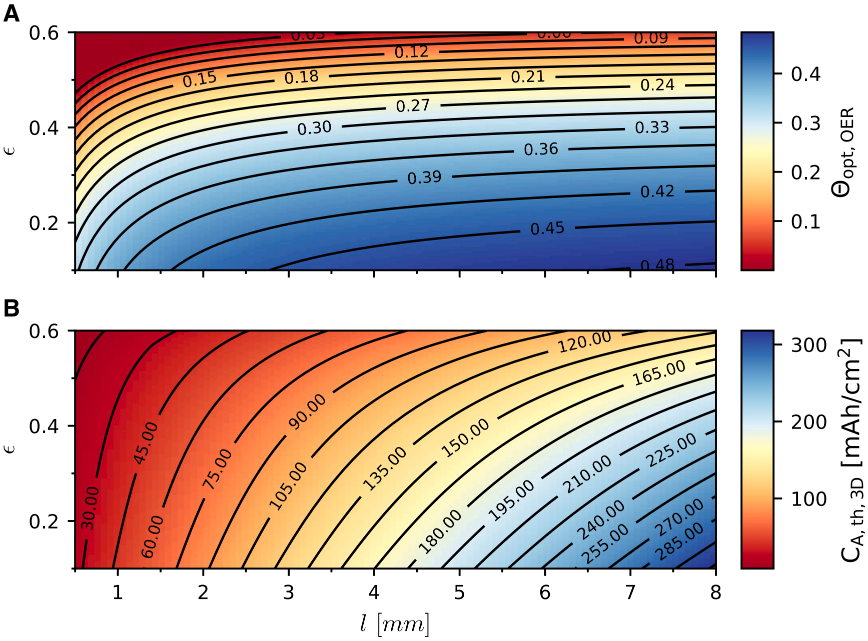

Figure 10. Optimal void fraction for the OER and resulting theoretical capacities

(A) Optimal void fraction $(\Theta_{opt,OER})$ with respect to the OER for varying electrode thicknesses *l* and porosities ε after active material loading.

(B) Resulting theoretical areal capacities $(C_{A,th,3D})$ that can be loaded onto a 3D electrode with an initial porosity of $\varepsilon_0 = 0.75$ before active material loading and a void fraction of $\Theta_{opt,OER}$. The charge rate is 200 mA/cm^2.

activation overpotentials. Therefore, in order to minimize overpotentials, the void fraction must be chosen to maximize the effectively utilized reactive surface over which the applied current is distributed. Using the 1D model, we determine the electrode utilization and polarization for oxygen evolution for different electrode thicknesses, porosities, and void fractions. We find simple relationships between the dimensionless parameters of utilization *U*, reduced polarization Φ, reduced total current *I*, and resistance parameter *K* that allow for the fast assessment of an electrode's performance at a given current density.

Based on these dimensionless relationships, we develop a method to calculate the optimal electrode void fraction for a given electrode thickness, porosity, and current density that minimizes the electrode polarization for oxygen evolution. Void fractions of up to around 0.50 are especially beneficial for oxygen evolution in thick electrodes with porosities below around 0.62 and at high current densities. A 3D geometry can not only reduce electrode polarization during oxygen evolution but also significantly improve the charging efficiency as a result of the more homogeneous current distribution. However, these benefits must be weighed against the lower theoretical areal capacity of 3D electrodes under consideration of the operating conditions and requirements for energy storage and oxygen evolution.

The void fraction of 3D electrodes constitutes a novel degree of freedom in the development of battery-electrolyzer electrodes. As such, it allows for the rational design of electrodes across a spectrum ranging from an emphasis on battery to electrolysis functionality. Even though our analysis neglects effects of bubbles as well as electrical and mass transfer resistances, the methods developed in this work allow for a first assessment of how electrode porosity, thickness, and void fraction affect performance metrics such as utilization, polarization, and charging efficiency.

METHODS

Model implementation

The dimensionless differential Equations 9 and 22 were solved via the finite difference method implemented in Python version 3.8.5. To accelerate computation, we used the Cython programming language that optimizes Python code by compiling it into C.[52] All computations were performed on an Alienware Aurora R13 PC with an intel CORE i7 processor. The model implementation was validated for OER by comparison with the results of Posey.[36] Modeling parameters are listed in Table S1.

RESOURCE AVAILABILITY

Lead contact

Requests for further information and resources should be directed to and will be fulfilled by the lead contact, Fokko M. Mulder (f.m.mulder@tudelft.nl).

Materials availability

This study did not generate new materials.

Data and code availability

- Experimental data of Möller-Gulland and Mulder[34] are available in the repository https://doi.org/10.4121/a87a59f5-e43a-4527-b047-dd6fb766b31b.
- The code generated during this study is available in the same repository.
- Any additional information required to reanalyze the data reported in this paper is available from the lead contact upon request.

ACKNOWLEDGMENTS

This work is part of the Open Technology research program with project no. 15169, which is (partly) financed by the Netherlands Organisation for Scientific Research (NWO).

AUTHOR CONTRIBUTIONS

Conceptualization, R.M.-G. and F.M.M.; porous electrode model development, investigation, and data analysis, R.M.-G.; writing – original draft, R.M.-G.; writing – review & editing, R.M.-G., J.R.v.O., and F.M.M.; project funding and initialization, F.M.M.

DECLARATION OF INTERESTS

A patent was submitted based on the current work by R.M.-G. and F.M.M. F.M.M. is co-founder of Battolyser Systems, a TU Delft spin-off company for the commercialization of battolyser^{TM} technology.

SUPPLEMENTAL INFORMATION

Supplemental information can be found online at https://doi.org/10.1016/j.xcrp.2025.102545.

Received: October 28, 2024
Revised: January 24, 2025
Accepted: March 21, 2025
Published: April 16, 2025

REFERENCES

1. Wheeler, T., and Von Braun, J. (2013). Climate change impacts on global food security. Science *341*, 508–513.
2. Trisos, C.H., Merow, C., and Pigot, A.L. (2020). The projected timing of abrupt ecological disruption from climate change. Nature *580*, 496–501.
3. Diffenbaugh, N.S., and Burke, M. (2019). Global warming has increased global economic inequality. Proc. Natl. Acad. Sci. USA *116*, 9808–9813.
4. Robinson, W.A. (2021). Climate change and extreme weather: A review focusing on the continental United States. Journal of the Air & Waste Management Association *71*, 1186–1209.
5. Mulder, F.M. (2014). Implications of diurnal and seasonal variations in renewable energy generation for large scale energy storage. J. Renew. Sustain. Energy *6*, 033105.
6. Denholm, P., Arent, D.J., Baldwin, S.F., Bilello, D.E., Brinkman, G.L., Cochran, J.M., Cole, W.J., Frew, B., Gevorgian, V., Heeter, J., et al. (2021). The challenges of achieving a 100% renewable electricity system in the united states. Joule *5*, 1331–1352.
7. Mulder, F.M., Weninger, B.M.H., Middelkoop, J., Ooms, F.G.B., and Schreuders, H. (2017). Efficient electricity storage with a battolyser, an integrated Ni–Fe battery and electrolyser. Energy Environ. Sci. *10*, 756–764.
8. Newman, J., and Tiedemann, W. (1975). Porous-electrode theory with battery applications. AIChE J. *21*, 25–41.
9. Haverkort, J.W. (2019). A theoretical analysis of the optimal electrode thickness and porosity. Electrochim. Acta *295*, 846–860.
10. Roy, T., Salazar de Troya, M.A., Worsley, M.A., and Beck, V.A. (2022). Topology optimization for the design of porous electrodes. Struct. Multidiscipl. Optim. *65*, 171.
11. Zeng, L., Li, P., Yao, Y., Niu, B., Niu, S., and Xu, B. (2020). Recent progresses of 3D printing technologies for structural energy storage devices. Materials Today Nano *12*, 100094.
12. Xu, X., Tan, Y.H., Ding, J., and Guan, C. (2022). 3D printing of next-generation electrochemical energy storage devices: from multiscale to multimaterial. Energy &. Environ. Materials *5*, 427–438.
13. Mooraj, S., Qi, Z., Zhu, C., Ren, J., Peng, S., Liu, L., Zhang, S., Feng, S., Kong, F., Liu, Y., et al. (2021). 3D printing of metal-based materials for renewable energy applications. Nano Res. *14*, 2105–2132.
14. Saleh, M.S., Li, J., Park, J., and Panat, R. (2018). 3D printed hierarchically-porous microlattice electrode materials for exceptionally high specific capacity and areal capacity lithium ion batteries. Addit. Manuf. *23*, 70–78.
15. Kong, D., Wang, Y., Huang, S., Zhang, B., Lim, Y.V., Sim, G.J., Valdivia y Alvarado, P., Ge, Q., and Yang, H.Y. (2020). 3d printed compressible quasi-solid-state nickel–iron battery. ACS Nano *14*, 9675–9686.
16. Li, C., Du, J., Gao, Y., Bu, F., Tan, Y.H., Wang, Y., Fu, G., Guan, C., Xu, X., and Huang, W. (2022). Stereolithography of 3d sustainable metal electrodes towards high-performance nickel iron battery. Adv. Funct. Mater. *32*, 2205317.
17. Kou, T., Wang, S., Shi, R., Zhang, T., Chiovoloni, S., Lu, J.Q., Chen, W., Worsley, M.A., Wood, B.C., Baker, S.E., et al. (2020). Periodic porous 3D electrodes mitigate gas bubble traffic during alkaline water electrolysis at high current densities. Adv. Energy Mater. *10*, 2002955.
18. Sullivan, I., Zhang, H., Zhu, C., Wood, M., Nelson, A.J., Baker, S.E., Spadaccini, C.M., Van Buuren, T., Lin, M., Duoss, E.B., et al. (2021). 3D printed nickel–molybdenum-based electrocatalysts for hydrogen evolution at low overpotentials in a flow-through configuration. ACS Appl. Mater. Interfaces *13*, 20260–20268.
19. Bui, J.C., Davis, J.T., and Esposito, D.V. (2020). 3d-printed electrodes for membraneless water electrolysis. Sustain. Energy Fuels *4*, 213–225.
20. Márquez, R.A., Kawashima, K., Son, Y.J., Rose, R., Smith, L.A., Miller, N., Carrasco Jaim, O.A., Celio, H., and Mullins, C.B. (2022). Tailoring 3d-printed electrodes for enhanced water splitting. ACS Appl. Mater. Interfaces *14*, 42153–42170.
21. Vogt, H. (2012). The actual current density of gas-evolving electrodes—notes on the bubble coverage. Electrochim. Acta *78*, 183–187.
22. Bongenaar-Schlenter, B.E., Janssen, L.J.J., Van Stralen, S.J.D., and Barendrecht, E. (1985). The effect of the gas void distribution on the ohmic resistance during water electrolytes. J. Appl. Electrochem. *15*, 537–548.
23. Swiegers, G.F., Terrett, R.N.L., Tsekouras, G., Tsuzuki, T., Pace, R.J., and Stranger, R. (2021). The prospects of developing a highly energy-efficient water electrolyser by eliminating or mitigating bubble effects. Sustain. Energy Fuels *5*, 1280–1310.
24. De Vidts, P., and White, R.E. (1995). Mathematical modeling of a nickel-cadmium cell: Proton diffusion in the nickel electrode. J. Electrochem. Soc. *142*, 1509–1519.
25. Fan, D., and White, R.E. (1991). Mathematical modeling of a nickel-cadmium battery: Effects of intercalation and oxygen reactions. J. Electrochem. Soc. *138*, 2952–2960.
26. Gu, W.B., Wang, C.Y., Li, S.M., Geng, M.M., and Liaw, B.Y. (1999). Modeling discharge and charge characteristics of nickel–metal hydride batteries. Electrochim. Acta *44*, 4525–4541.
27. Mao, Z., De Vidts, P., White, R.E., and Newman, J. (1994). Theoretical analysis of the discharge performance of a NiOOH/H 2cell. J. Electrochem. Soc. *141*, 54–64.
28. Li, H., Bucci, G., Brady, N.W., Cross, N.R., Ehlinger, V.M., Lin, T.Y., Salazar de Troya, M., Tortorelli, D., Worsley, M.A., and Roy, T. (2024). Topology optimization for the full-cell design of porous electrodes in electrochemical energy storage devices. Struct. Multidiscipl. Optim. *67*, 188.
29. Reale Batista, M.D., Chandrasekaran, S., Moran, B.D., Salazar de Troya, M., Pinongcos, A., Wang, Z., Hensleigh, R., Carleton, A., Zeng, M., Roy, T., et al. (2023). Design and additive manufacturing of optimized electrodes for energy storage applications. Carbon *205*, 262–269.
30. Beck, V.A., Wong, J.J., Jekel, C.F., Tortorelli, D.A., Baker, S.E., Duoss, E.B., and Worsley, M.A. (2021). Computational design of microarchitected porous electrodes for redox flow batteries. J. Power Sources *512*, 230453.
31. Paxton, B., and Newman, J. (1997). Modeling of nickel/metal hydride batteries. J. Electrochem. Soc. *144*, 3818–3831.
32. Kadyk, T., Bruce, D., and Eikerling, M. (2016). How to enhance gas removal from porous electrodes? Sci. Rep. *6*, 38780.
33. Tjaden, B., Cooper, S.J., Brett, D.J., Kramer, D., and Shearing, P.R. (2016). On the origin and application of the bruggeman correlation for analysing transport phenomena in electrochemical systems. Current opinion in chemical engineering *12*, 44–51.

Please cite this article in press as: Möller-Gulland et al., Modeling 3D hybrid battery-electrolyzer nickel electrodes, Cell Reports Physical Science (2025), https://doi.org/10.1016/j.xcrp.2025.102545

34. Möller-Gulland, R., and Mulder, F.M. (2024). 3d nickel electrodes for hybrid battery and electrolysis devices. Cell Reports Physical Science *5*, 10228.
35. Daniel'-Bek, V.S. (1948). Polarization of porous electrodes I. distribution of current and potential within the electrode. Zh. Fiz. Khim. *22*, 697.
36. Posey, F.A. (1964). Methods for the calculation of polarization in porous electrodes. J. Electrochem. Soc. *111*, 1173.
37. Raventos, A.M., Kluivers, G., Haverkort, J.W., De Jong, W., Mulder, F.M., and Kortlever, R. (2021). Modeling the performance of an integrated battery and electrolyzer system. Ind. Eng. Chem. Res. *60*, 10988–10996.
38. Motupally, S., Streinz, C.C., and Weidner, J.W. (1998). Proton diffusion in nickel hydroxide: prediction of active material utilization. J. Electrochem. Soc. *145*, 29–34.
39. Ta, K.P., and Newman, J. (1998). Mass transfer and kinetic phenomena at the nickel hydroxide electrode. J. Electrochem. Soc. *145*, 3860–3874.
40. Conway, B.E., and Gileadi, E. (1962). Electrochemistry of the nickel oxide electrode: part iv. electrochemical kinetic studies of reversible potentials as a function of degree of oxidation. Can. J. Chem. *40*, 1933–1942.
41. Gomadam, P.M., Weidner, J.W., Dougal, R.A., and White, R.E. (2002). Mathematical modeling of lithium-ion and nickel battery systems. J. Power Sources *110*, 267–284.
42. Santos, D.M.F., Sequeira, C.A.C., and Figueiredo, J.L. (2013). Hydrogen production by alkaline water electrolysis. Quim. Nova *36*, 1176–1193.
43. Shukla, A.K., Ravikumar, M.K., and Balasubramanian, T.S. (1994). Nickel/iron batteries. J. Power Sources *51*, 29–36.
44. Rausch, S., and Wendt, H. (1996). Morphology and utilization of smooth hydrogen-evolving raney nickel cathode coatings and porous sintered-nickel cathodes. J. Electrochem. Soc. *143*, 2852–2862.
45. Liu, M.-B., Cook, G.M., and Yao, N.P. (1982). Transient current distributions in porous zinc electrodes in KOH electrolyte. J. Electrochem. Soc. *129*, 239–246.
46. Lengyel, I.M., Soroldoni, D., Oates, A.C., and Morelli, L.G. (2014). Nonlinearity arising from noncooperative transcription factor binding enhances negative feedback and promotes genetic oscillations. Pap. Phys. *6*. 060012–0.
47. Yazvinskaya, N.N., Galushkin, N.E., Galushkin, D.N., and Kalmykov, B.Y. (2020). Analysis and comparison of generalized Peukert's equations parameters for nickel-cadmium batteries with pocket and sintered electrodes. Int. J. Electrochem. Sci. *15*, 412–423.
48. Zimmerman, A.H. (1984). Technological implications in studies of nickel electrode performance and degradation. J. Power Sources *12*, 233–245.
49. Oshitani, M., Sasaki, Y., and Takashima, K. (1984). Development of a nickel electrode having stable performance at various charge and discharge rates over a wide temperature range. J. Power Sources *12*, 219–231.
50. Yuan, A., Cheng, S., Zhang, J., and Cao, C. (1998). The influence of calcium compounds on the behaviour of the nickel electrode. J. Power Sources *76*, 36–40.
51. Zeng, K., and Zhang, D. (2010). Recent progress in alkaline water electrolysis for hydrogen production and applications. Prog. Energy Combust. Sci. *36*, 307–326.
52. Behnel, S., Bradshaw, R., Citro, C., Dalcin, L., Seljebotn, D.S., and Smith, K. (2011). Cython: The best of both worlds. Comput. Sci. Eng. *13*, 31–39.